Direct-Write 3D-Nanoprinting of Plasmonic Structures

Robert Winkler[1], Franz-Philipp Schmidt[1,2], Ulrich Haselmann[1], Jason D. Fowlkes[3,4], Brett B. Lewis[3,4], Gerald Kothleitner[1,5], Philip D. Rack[3,4,+], Harald Plank[1,5,]*

[1] Graz Centre for Electron Microscopy, Steyrergasse 17, 8010 Graz, AUSTRIA

[2] Institute of Physics, Karl-Franzens-University, Universitätsplatz 5, 8010 Graz, AUSTRIA

[3] Center for Nanophase Materials Sciences, Oak Ridge National Laboratory, Oak Ridge, Tennessee 37831, USA

[4] Department of Materials Science and Engineering, University of Tennessee, Knoxville, Tennessee 37996, USA

[5] Institute of Electron Microscopy and Nanoanalysis, Graz University of Technology, 8010 Graz, AUSTRIA

* corresponding author: E-mail: harald.plank@felmi-zfe.at

[+] co-corresponding author: E-mail: prack@utk.edu

Abstract

During the last decade, significant progress has been made in the field of resonant optics ranging from fundamental aspects to concrete applications. While several techniques have been introduced for the fabrication of highly defined metallic nanostructures, the synthesis of complex, free-standing 3-dimensional (3D) structures is still an intriguing, but so far intractable challenge. In this study we demonstrate a 3D direct-write synthesis approach which addresses this challenge. Specifically, we succeeded in the direct-write fabrication of 3D nano-architectures via electron stimulated reactions which is applicable on virtually any material and surface morphology. By that, complex 3D nano-structures composed of highly compact, pure gold can be fabricated which reveal strong plasmonic activity paving the way for a new generation of 3D nano-plasmonic architectures that can be printed on-demand.

KEYWORDS: focused electron beam induced deposition, 3D nanoprinting, plasmonics, gold, purification, nanofabrication, surface plasmon resonance, nanostructures

Introduction

Surface plasmons in metallic nanostructures are known to have unique properties as they enable light concentration into the deep subwavelength regime. They are thus of high interest for new types of photonic devices[1] such as novel light sources[2], sensor devices[3,4], for improvements in data storage technology[5], and in photovoltaics[6]. A high flexibility for the design of the metallic nanostructures is therefore in high demand. Several factors affect the plasmonic activity, namely: ***1)*** the shape and size of the metallic nanostructure, ***2)*** the quality of the metal in terms of its purity and crystallinity, and ***3)*** accurate positioning on the area of interest. Different approaches have been used so far, but it is very challenging to meet all these requirements. On one hand, wet chemical synthesis enables the production of single crystalline nanoparticles with well-defined shape and high metallic purity[7,8]. However, accurate positioning on the substrate – particularly an arrangement of multiple nanoparticles with tuneable, well-defined relative distances – is not possible. On the other hand, electron beam lithography (**EBL**) overcomes this positioning problem but is limited to quasi two dimensional structures and flat surfaces. While these challenges are daunting, Focused Electron Beam Induced Deposition (**FEBID**) has the potential to meet these stringent requirements as it is a mask-less, direct-write bottom-up synthesis method for the fabrication of 1D, 2D, and 3D architectures with spatial nanometer resolution[9–12] on virtually any substrate material and surface morphology[13]. FEBID uses gaseous precursors, injected in electron beam microscopes, which dynamically physisorb, diffuse, and desorb to establish an equilibrium surface coverage. The focused electron beam decomposes the precursor molecules leading to a highly localized functional deposit whose size, shape, and position can be precisely controlled on the lower nanometer scale. In the past, FEBID has been used to rapidly prototype passive and active applications[14–18] and has already found its way into commercial applications for lithography mask repair[19,20] or stress-strain sensing for atomic force microscopy cantilevers[21,22]. However, FEBID deposits notoriously contain very high carbon content of 90 at.% and more for some precursors after fabrication which compromise the intended functionality[23]. Although a few examples of pure materials after fabrication have been

demonstrated[23–26] most efforts were put on *in-situ* and/or *post-growth* purification processes such as: fabrication on hot substrates[25,27], co-flow with reactive gases[28], synchronized laser assisted FEBID[29,30] and other *in-situ*/*ex-situ* processes[21,23,31–37]. An essential step forward was achieved by Geier et-al who introduced the first post-growth purification approach for platinum based FEBID materials leading to pure and highly compact metallic nano-structures without morphological disruption[38]. In this study we successfully expand their basic purification concept to a gold-based FEBID precursor and, more importantly, to complex free-standing 3D architectures - a much more challenging task than with simple planar or bulky 3D structures. This chemical post-growth transfer into highly compact, pure gold is then combined with one of FEBID's unique attributes by means of direct-write 3D fabrication. In the past, this capability was mostly restricted to free-standing nano-pillars for detailed insight in fundamental processes[24,39–41]. While Fowlkes et-al recently succeeded in mimicking experimental 3D fabrication via simulations[42] we here move an essential step further and demonstrate FEBID based fabrication of complex and highly precise 3D nano-architectures which meets the high demands for advanced plasmonic applications after the successful chemical transformation into pure gold. The roadmap of this study is graphically summarized in Figure 1. First, we report on our recent breakthrough progress towards real 3D nanoprinting of complex, freestanding 3D-nanoarchitectures (top row, a-e) by using advanced patterning strategies. Next, we demonstrate the chemical material transfer of carbon containing FEBID deposits into highly compact pure Au nano-structures (central row, f-h). Then we confirm the plasmonic response of planar FEBID based Au structures which reproduce the response of reference Au disks prepared via classical electron beam lithography[43] (bottom row, i-l). This not only fulfills the long lasting promise of FEBID as fabrication tool for plasmonic nano-strutures but also paves the way for FEBID based 3D plasmonics. Hence, in the last step we adapt the purification process for the carbon removal in 3D nano-structures and successfully demonstrate the plasmonic activity of free-standing 3D Au nano-architectures (bottom row, m-o) whose fabrication is extremely challenging or even impossible with alternative techniques. By that, the proposed approach opens the possibility of entirely new

capabilities for the on-demand fabrication of 3D architectures for resonant optics on virtually any surface.

3D-Nanoprinting

In the last decade, FEBID has made significant, yet incremental progress towards synthesis of freestanding nano-structures[44,45]. Together with a deeper understanding of the dynamic surface processes concerning precursor molecule adsorption, diffusion and desorption and its relation to the process parameters[46–49] we recently succeeded in the identification of a widely stable process window where the intended 3D nano-structures becomes very predictable, preventing exhaustive trial-and-error approaches mostly used in the past[42]. In previous experiments, we determined that high primary electron beam energies (30 keV), low beam currents (21 pA) in combination with pixel distances (point pitch, **PoP**) in the (sub)nanometer range and pulse durations (dwell times, **DT**) on a millisecond scale are ideal for 3D synthesis. While general control over tilt angles of free-standing 3D structures is achieved by careful variation of PoPs and DTs, the patterning point sequence is the essential element for predictable and reproducible 3D fabrication. Although the primary beam parameters lead to minimized local precursor depletion during a beam pulse[9,50,51], continuous growth mode for individual branches lead to varying growth rates dependent on the height making the result unpredictable. Figure 2a shows a top view and a tilted SEM image after a fabrication attempt for a tetragonal-bipyramid (**TBP**, as depicted in in Figure 1g) using a continuous growth mode. As schematically given on top, this strategy tries to grow each single branch individually (see number and arrows). One reason for the structural collaps is attributed to increasing local depletion leading to strongly reduced growth followed by new growth events at the substrate. To prevent such a situation, patterning has been changed to an interlaced patterning sequence as schematically depicted on top of Figure 2b. This strategy jumps between different branches (see numbers and arrows), essentially introducing sufficient refresh times in between two consecutive beam pulses at

the same branch. This establishes a replenished growth front prior to the next beam pulse, leading to a stable growth mode as can be seen by the TBP in Figure 2a (both attempts used the same DTs and PoPs without any additional pause times). At the same time, this strategy mitigates proximity effects that produce spatial distortions[39,52] and drift issues (further details can be found in Supporting Information 1). Following this interlace approach, even complex 3D-nanostructures, as representatively shown in Figure 1a-e, can be fabricated in a predicatable, reliable, reproducible fashion (see also Supporting Information 1). These examples demonstrate FEBID´s high flexibility concerning the fabrication of 3D nano-architectures which exploit their full potential together with applicability on virtually any surface material and morphology (more examples can be found in Supporting Information 2). To demonstrate FEBID based 3D plasmonics in this study, tetragonal-bipyramid geometries consisting of 4 individual branches that converge in the vertical dimension into a single apex have been chosen (see Figure 1g, 1n, and 2b). The intension of this geometry are the expected enhanced plasmonic resonances at branch areas and in particular at the tip[53] with typically end radii of ~10 nm. However, for strong plasmonic resonance the critical issue of carbon impurities in the 3D gold deposits had to be solved first as discussed in the following.

Material Purity for Plasmonics

Although a variety of precursor materials are available for FEBID[23], most of them lead to a carbon matrix composition embedded with metal nano-grains (2 - 5 nm) (see Figure 1f) with an enormous C contents depending on the organometallic precursor composition (e.g. the Au precursor used here contains about 95 at.% carbon[23]). This long-lasting drawback reduces or even entirely masks the intended magnetic, electric, or plasmonic functionality. Here we successfully solved the impurity problem with a post-growth purification approach for the $Me_2Au(acac)$ (acetylacetonate- dimethyl-gold(III) precursor to obtain pure gold materials as a central gateway for plasmonic applications. Specifically, the as-deposited Au-C FEBID structures are exposed to a scanning e-beam in a 10 Pa H_2O

ambient in an environmental scanning electron microscope[38] (**ESEM**) (Figure 1g). A comprehensive characterization of such treated Au-C deposits using atomic force microscopy (**AFM**), scanning electron microscopy (**SEM**) based energy dispersive X-ray spectroscopy (**EDXS**) and transmission electron microscopy (**TEM**) based electron energy loss spectroscopy (**EELS**) not only revealed the entire removal of carbon but also the pore / crack free morphology after purification which is essential for plasmonic application (see Supporting Information 3). To evaluate the latter aspect, we fabricated two sets of 60 nm thick Au-C FEBID disks with diameters ranging from 250 nm to 400 nm, all deposited on 15 nm thick Si_3N_4 membranes for subsequent EELS characterization. One set was used for as-deposited characterization, while the second disk set was purified via the above described approach. In addition, a third set of Au reference disks with same diameters and thickness were prepared using electron beam lithography (**EBL**)[54] to evaluate the behaviour of FEBID based Au disks as described in the following.

2D Plasmonics

To study the plasmonic behaviour of planar FEBID Au disks, TEM based nano-characterization has been performed as it provides energy dependent response information with laterally resolved information on the lower nanoscale. Figure 3 shows scanning transmission electron microscopy (**STEM**) based high-angle annular dark field (**HAADF**) survey images (left column in Figure 2a) together with EELS measurements of the laterally resolved plasmonic response of FEBID based as-deposited Au-C (top row) and fully purified Au (central row) in comparison with EBL based Au reference disks[55–58]. As evident, as-deposited Au-C disks (top row) do not produce a plasmonic response at any electron loss energy (A → D). However, fully purified Au FEBID disks (central row) clearly reveal surface plasmon resonances. A direct comparison of the EEL signal originating from the disk centre of as-deposited and fully purified FEBID disks (see indication in column D in Figure 3a) is given in Figure 3b. Note, the central plasmon activity indicates the presence of the so-called

breathing mode[43] which is characteristic for such geometries. Comparing the purified FEBID disks (central row) with the Au EBL reference disks (bottom row) a very similar qualitative behaviour is observed[43,59]. Starting at low energies the expected dipole (A), quadrupole (B) and hexapole (C) resonances are clearly observed [55–58]. In addition, the breathing mode (D) is observed for both fabrication methods. As expected, distinct peak shifts to higher energies were observed with decreasing disk size as shown in the EEL spectra in Figure 3c for pure FEBID disks (left) and Au EBL reference disks (right). Here EEL spectra originating from the edge region along the disk circumference are displayed. While the dipole (A) and quadrupole mode (B) are well resolved in both set of spectra, the hexapole mode (C) is only visible in the EBL reference data set for the larger disk diameters. The corresponding EEL map (C) at an energy of 1.6 eV in Figure 3a (centre row), however, clearly shows a ring shaped distribution similar to the hexapolar EEL map of the EBL reference (bottom row) which confirms the formation of the hexapole mode in fully purified FEBID disks as expected. The main differences between FEBID and EBL disks are two-fold. First, slightly less pronounced plasmonic peaks are observed for the fully purified FEBID disks (Figure 3c, left curves). The reduction in peak sharpness and intensity originates from the slightly rougher edges for purified FEBID disks as evident in the HAADF image in Figure 3a. As this is equivalent to a superposition of slightly different diameters within one structure, the peaks in the EEL spectra are broader and less intense. The second deviation between EBL and FEBID disks is a general peak shift to lower energies for purified structures. We attribute this effect to the smaller nano-grain sizes for FEBID based materials as reported in literature before[60] but also to very small nano-voids possibly formed during fabrication and / or purification. Despite these slight deviations, these results clearly demonstrate that fully purified FEBID based Au disks exhibit the critical characteristics required for plasmonic applications. Besides the fact that we here fulfilled the long lasting promise of FEBID concerning the on-demand fabrication of plasmonically active Au nanostructures, this achievement paves the way for the expansion to free-standing 3D arachitectures as first ever demonstrated in the following.

3D Plasmonics

First, free-standing, TBPs have been synthesized via FEBID´s 3D-nano-printing capabilities as shown by TEM and SEM images in Figure 1g, 1n, 2b and 4a. These 3D Au-C TBPs were then transferred into pure gold via the electron-stimulated H_2O purification process described above. Although free-standing 3D purification requires higher electron doses as well as reduced dwell times and lower purification rates to prevent structural collapsing (see Supporting Information 4), this approach is capable of yielding intact 3D TBP geometries as shown Figure 4a. High-resolution TEM (Figure 4b) confirms the highly compact inner structure, reveals branch diameters of approximately 25 nm and indicates minimal surface contamination after the purification process of less than 1 nm. In preparation for plasmonic characterization via STEM-EELS, pure gold TBP structures were fabricated on copper TEM grids with a 300 nm thick insulating SiO_X[23] spacer layer (see Supporting Information 1) to prevent electrical contact between TBPs and the substrate. As summarized in Figure 5, fully purified Au TBPs reveal strong plasmonic activity, while no plasmonic response was observed for as-deposited Au-C TBPs. Specifically, Figure 5a gives a HAADF survey image of a fully purified 3D TBP structure together with correlated and deconvolved EEL maps at different electron loss energies in Figure 5b-d which confirms the surface plasmon resonances (see also Supporting Video). The first noteworthy detail is the symmetric appearance of plasmon modes across the TBP structure which exhibits the precision of initial FEBID fabrication and the minimally disrupting purification procedure with respect to the local dimensions (see Supporting Information 4). As intended by the TBP design, highest plasmonic activity was found at the branching areas and the tip region due to superpositioned oscillations from the involved branches (see Figure 5 and Supporting Video). This becomes also evident in Figure 6 which shows two unprocessed raw EEL spectra taken from two different regions-of-interest at a free-standing double-branch structure as evident from the survey image (inset top right). The corresponding EEL maps were taken from 0.68 eV and 1.29 eV (see dashed lines at the red and blue curve, respectively) which again reveals the highly localized plasmonic activity. Particularly noteworthy is the fact that even the here shown as-acquired raw data

clearly reveal the plasmon peaks further indicates the high material quality after purification (Figure 6). Together with FEBIDs high flexibility in overall and local 3D design (see Figure 1a-e and Supporting Information 2) the here proposed 3D nano-printing approach might open up entirely new possibilities for fundamental science in the field of optical resonance beyond current limitations.

Conclusion

The application of free-standing, 3-dimensional, plasmonically active architectures with spatial nanometer resolution strongly relies on proper synthesis methods. Although different approaches have been used to generate plasmonic nanostructures, they are restricted to precisely placed quasi planar features in the case of lithographically methods or complex geometries with no ability to control their placement in the case of wet chemical processing. Here we successfully demonstrated an innovative direct-write, bottom-up synthesis approach which allows the on-demand fabrication of complex, free-standing 3D nano-structures composed of pure gold for plasmonic applications. The latter can range from device oriented integration on practically any surface towards fundamentally oriented studies concerning 3D plasmonics which, e.g. in combination with 3D TEM tomography, might enable entirely new physical insights. Beyond plasmonics, FEBID based 3D nano-printing can be considered as a generic approach for nanoscale 3D fabrication with the potential to push the limits of nanoscale optical, mechanical, magnetic, and even multi-functional 3D metamaterials beyond current limitations.

Methods

Fabrication general: focused electron beam induced deposition (**FEBID**) was performed on a NOVA 200 dual beam instrument (FEI, The Netherlands) equipped with 5 FEI gas injection systems (**GIS**). Silicon dioxide was deposited from Tetraethyl orthosilicate (TEOS, CAS: 78-10-4), inserted via a nozzle at 52° with relation to the substrate and a vertical distance of 120 µm. For Au-C deposition the precursor material $Me_2Au(acac)$ (acetylacetonate- dimethyl-gold(III), CAS: 14951-50-9) and for Pt-C deposits $MeCpPt(IV)Me_3$ (CAS: 94442-22-5) was used with similar spatial arrangement. Au- and Pt-based precursors were heated to 30° and 45°C, respectively, for at least 30 minutes prior to any deposition. The long axes of the GIS nozzles were aligned in such way that they coincide with the beam centre. The nozzle angles with relation to the surface were 52° for Au and 38° for the Pt-GIS. For a symmetrical gas replenishment situation, scan rotation was applied in such way that scan direction was perpendicular to the nozzle main axes. Beam focusing was carefully done at high magnification by deposition of small pillars (5 seconds) in close proximity to the region of interest until pillar diameters below 40 nm and 50 nm for Au and Pt, respectively, were achieved in top view. Prior to any deposition the stage was not moved for at least 15 minutes and gas flux was turned on for at least 5 minutes before any fabrication step. In general, electron exposure of the region of interest was reduced to a minimum in order to prevent contamination. Base pressure of the dual beam chamber was $3*10^{-6}$ mbar while the background pressure increase to $6*10^{-6}$ mbar and $1*10^{-5}$ mbar for Au- and Pt-based precursor, respectively. For preliminary purification tests, FEBID structures were deposited on carefully pre-cleaned 1x1 cm² silicon wafer with a 3 nm SiO_2 top layer.

Fabrication of Au-pads and -disks: 2x2 µm² Au-C pads with heights ranging from 60-150 nm were deposited with 5 keV, 1600 pA, 100 µs dwell time, 13 nm point pitch using serpentine scanning with the slow scan axis direct towards the GIS (these pads were used for purification studies as discussed in Supporting Information 3). Au-disks for plasmonics were fabricated with 30 keV, 150 pA, 5 ms dwell time, and 5 nm point pitch using serpentine strategies with the slow scan axis directed to the GIS. All disks were directly fabricated on plasma pre-cleaned TEM grids with 15 nm thick Si_3N_4

membranes (Ted Pella; Prod-Nr: 21569-10). Gold reference nano-disks were prepared by electron beam lithography (**EBL**) in a RAITH e-line system using a poly(methylmetacrylate) resist on a 15 nm thick Si_3N_4 membrane and a standard gold evaporation and lift-off procedure[54].

Tetragonal-bipyramids fabrication: A copper TEM grid with a rectangle hole was cut into half and clamped flat on a specimen holder. For a better visibility in the ESEM and correlation of the fabricated structures at the TEM, slits in a distance of about 20 µm were initially milled with the focused ion beam using 30 kV, 20 nA and 52° stage tilt. The grid was then mounted upright in a SEM stab and both edges chamfered for 12° (30 kV, 5 nA, stage tilt 40°) to remove any material that might cast a shadow during TEM investigations. Next, silicon dioxide squares (1.5 x 1.5 µm², 300 nm in height) were deposited from Tetraethyl orthosilicate (TEOS) precursor in combination with H_2O water at primary energy of 5 kV and a beam current of 6.3 nA. Finally, small markers were cut (30 kV, 500 pA), indicating the location of the pads to ensure visibility in ESEM mode. TBP fabrication was done at 30 keV, 21 pA and a PoP of 0.5 nm using the parameters and patterning strategies specified in the Supporting Information 1.

Purification: purification was done in a QUANTA 200 ESEM (FEI, The Netherlands) right after fabrication. The beam current was determined with a Faraday cup in high-vacuum mode, purification was performed in ESEM-mode at a water vapour pressure of 10 Pa stabilized for at least 30 minutes prior to purification without e-beam exposure. Au-C pads were purified with primary energy of 5 keV, a beam current of 1.9 nA, a point pitch of 6 nm and a dwell time of 1 µs. Disks for plasmonic investigations were purified of 5 keV, 0.5 nA, a DT of 1 µs at a PoP of 6 nm. Total electron doses of 28 C\cm² were applied for all pads and disks. 3D purification was done at with 5 keV, 1.2 nA, a DT of 1 µs and a PoP of 4 nm. Electron doses varied from 5 C/cm² to 200 C/cm².

Characterization: AFM characterization was done with a FastScan Bio AFM microscope in tapping mode and soft repulsive conditions using AFM tips with spring constants of 4 N/m (Bruker AXS, CA, USA). Post-processing was done with Bruker Nanoscope software. EDXS was performed with a Si(Li)-

detector (XL-30 EDXS system; EDAX; USA) in a QUANTA 200 ESEM (FEI, The Netherlands). For C/Au ratio determination a semi-quantitative approach was used[35,36,38]. EELS measurements were performed in a FEI Tecnai F20 transmission electron microscope with a monochromated 200 keV electron beam of 100 - 150 meV energy spread (full-width-at-half-maximum, FWHM). EEL spectra were recorded in the STEM-EELS mode[58] with an energy dispersion of 10 meV/channel in a high resolution Gatan Imaging Filter equipped with a 2048x2048 pixel CCD camera. The EEL data shown in Figure 5 were further improved by a Richardson-Lucy deconvolution (MathWorks Matlab, deconvlucy function), implemented in a homemade analysis program ("SI analysis tool - A flexible MATLAB tool to analyse spectrum images", available at http://esteem2.eu in the section "Software"). All EEL maps shown in this work are integrated over an energy range of 100 meV.

Acknowledgements

RW, UH and HP gratefully acknowledge the valuable support by Prof. Dr. Ferdinand Hofer. Same authors also acknowledge financial support by the COST action CELINA (Nr. CM1301) and the EUROSTARS project TRIPLE-S (Nr. E! 8213). The research leading to these results has received funding from the EU FP7 programme [FP7/2007-2013] under grant agreement no. 312483 (ESTEEM2). PDR and JDF acknowledge that their contributions were supported by the Center for Nanophase Materials Sciences, which is sponsored at Oak Ridge National Laboratory by the Scientific User Facilities Division, Office of Basic Energy Sciences, U.S. Department of Energy.

NOTICE OF COPYRIGHT

References

(1) Barnes, W. L.; Dereux, A.; Ebbesen, T. W. Surface Plamons Subwavelength Optics. *Nature* **2003**, *424* (6950), 824–830.

(2) Okamoto, K.; Niki, I.; Shvartser, A.; Narukawa, Y.; Mukai, T.; Scherer, A. Surface-Plasmon-Enhanced Light Emitters Based on InGaN Quantum Wells. *Nat. Mater.* **2004**, *3* (9), 601–605.

(3) Lal, S.; Link, S.; Halas, N. J. Nano-Optics from Sensing to Waveguiding. *Nat. Photonics* **2007**, *1* (11), 641–648.

(4) Anker, J. N.; Hall, W. P.; Lyandres, O.; Shah, N. C.; Zhao, J.; Van Duyne, R. P. Biosensing with Plasmonic Nanosensors. *Nat. Mater.* **2008**, *7* (6), 442–453.

(5) Stipe, B. C.; Strand, T. C.; Poon, C. C.; Balamane, H.; Boone, T. D.; Katine, J. A.; Li, J.-L.; Rawat, V.; Nemoto, H.; Hirotsune, A.; Hellwig, O.; Ruiz, R.; Dobisz, E.; Kercher, D. S.; Robertson, N.; Albrecht, T. R.; Terris, B. D. Magnetic Recording at 1.5 Pb m−2 Using an Integrated Plasmonic Antenna. *Nat. Photonics* **2010**, *4* (7), 484–488.

(6) Atwater, H. A.; Polman, A. Plasmonics for Improved Photovoltaic Devices. *Nat. Mater.* **2010**, *9* (10), 865–865.

(7) Liz-Marza, L. M. Tailoring Surface Plasmons through the Morphology and Assembly of Metal Nanoparticles. *Langmuir* **2006**, *22* (22), 32–41.

(8) Grzelczak, Marek, Pérez-Juste, Jorge, Paul, Mulvaney, Liz-Marzán, L. M. Shape Control in Gold Nanoparticle Synthesis. *Chem. Soc. Rev.* **2008**, *37* (9), 1783–1791.

(9) Utke, I.; Russell, P. E. *Nanofabrication Using Focused Ion and Electron Beams: Principles and Applications.*; Oxford University Press: New York, **2012**.

(10) Utke, I.; Hoffmann, P.; Melngailis, J. Gas-Assisted Focused Electron Beam and Ion Beam Processing and Fabrication. *J. Vac. Sci. Technol. B Microelectron. Nanom. Struct.* **2008**, *26* (4), 1197–1276.

(11) Randolph, S. J.; Fowlkes, J. D.; Rack, P. D. Focused, Nanoscale Electron-Beam-Induced Deposition and Etching. *Crit. Rev. Solid State Mater. Sci.* **2006**, *31* (3), 55–89.

(12) Van Dorp, W. F.; Hagen, C. W. A Critical Literature Review of Focused Electron Beam Induced Deposition. *J. Appl. Phys.* **2008**, *104* (8), 81301–81342.

(13) Peinado, P.; Sangiao, S.; Teresa, J. M. De. Focused Electron and Ion Beam Induced Deposition on Flexible and Transparent Polycarbonate Substrates. *ACS Nano* **2015**, *9* (6), 6139–6146.

(14) Gabureac, M.; Bernau, L.; Utke, I.; Boero, G. Granular Co-C Nano-Hall Sensors by Focused-Beam-Induced Deposition. *Nanotechnology* **2010**, *21* (11), No. 115503.

(15) Kolb, F.; Schmoltner, K.; Huth, M.; Hohenau, A.; Krenn, J.; Klug, A.; List, E. J. W.; Plank, H. Variable Tunneling Barriers in FEBID Based PtC Metal-Matrix Nanocomposites as a Transducing Element for Humidity Sensing. *Nanotechnology* **2013**, *24* (30), No.

305501.

(16) Gavagnin, M.; Wanzenboeck, H. D.; Belić, D.; Bertagnolli, E. Synthesis of Individually Tuned Nanomagnets for Nanomagnet Logic by Direct Write Focused Electron Beam Induced Deposition. *ACS Nano* **2013**, *7* (1), 777–784.

(17) Perentes, A.; Bachmann, A.; Leutenegger, M.; Utke, I.; Sandu, C.; Hoffmann, P. Focused Electron Beam Induced Deposition of a Periodic Transparent Nano-Optic Pattern. *Microelectron. Eng.* **2004**, *73*, 412–416.

(18) Utke, I.; Jenke, M. G.; Röling, C.; Thiesen, P. H.; Iakovlev, V.; Sirbu, A.; Mereuta, A.; Caliman, A.; Kapon, E. Polarisation Stabilisation of Vertical Cavity Surface Emitting Lasers by Minimally Invasive Focused Electron Beam Triggered Chemistry. *Nanoscale* **2011**, *3* (7), 2718–2722.

(19) Edinger, K.; Becht, H.; Bihr, J.; Boegli, V.; Budach, M.; Hofmann, T.; Koops, H. W. P.; Kuschnerus, P.; Oster, J.; Spies, P.; Weyrauch, B. Electron-Beam-Based Photomask Repair. *J. Vac. Sci. Technol. B Microelectron. Nanom. Struct.* **2004**, *22* (6), 2902–2906.

(20) Lassiter, M. G.; Liang, T.; Rack, P. D. Inhibiting Spontaneous Etching of Nanoscale Electron Beam Induced Etching Features: Solutions for Nanoscale Repair of Extreme Ultraviolet Lithography Masks. *J. Vac. Sci. Technol. B Microelectron. Nanom. Struct.* **2008**, *26* (3), 963–976.

(21) Schwalb, C. H.; Grimm, C.; Baranowski, M.; Sachser, R.; Porrati, F.; Reith, H.; Das, P.; Müller, J.; Völklein, F.; Kaya, A.; Huth, M. A Tunable Strain Sensor Using Nanogranular Metals. *Sensors (Basel).* **2010**, *10* (11), 9847–9856.

(22) Porrati, F.; Sachser, R.; Schwalb, C. H.; Frangakis, A. S.; Huth, M. Tuning the Electrical Conductivity of Pt-Containing Granular Metals by Postgrowth Electron Irradiation. *J. Appl. Phys.* **2011**, *109* (6), No. 063715.

(23) Botman, A.; Mulders, J. J. L.; Hagen, C. W. Creating Pure Nanostructures from Electron-Beam-Induced Deposition Using Purification Techniques: A Technology Perspective. *Nanotechnology* **2009**, *20* (37), No. 372001.

(24) Klein, K. L.; Randolph, S. J.; Fowlkes, J. D.; Allard, L. F.; Meyer, H. M.; Simpson, M. L.; Rack, P. D. Single-Crystal Nanowires Grown via Electron-Beam-Induced Deposition. *Nanotechnology* **2008**, *19*, No. 345705.

(25) Córdoba, R.; Sesé, J.; De Teresa, J. M.; Ibarra, M. R. High-Purity Cobalt Nanostructures Grown by Focused-Electron-Beam-Induced Deposition at Low Current. *Microelectron. Eng.* **2010**, *87* (5–8), 1550–1553.

(26) Shawrav, M. M.; Taus, P.; Wanzenboeck, H. D.; Schinnerl, M.; Stöger-Pollach, M.; Schwarz, S.; Steiger-Thirsfeld, A.; Bertagnolli, E. Highly Conductive and Pure Gold Nanostructures Grown by Electron Beam Induced Deposition. *Sci. Rep.* **2016**, *6*, No. 34003.

(27) Mulders, J. J. L.; Belova, L. M.; Riazanova, A. Electron Beam Induced Deposition at Elevated Temperatures: Compositional Changes and Purity Improvement.

Nanotechnology **2011**, *22* (5), No. 055302.

(28) Langford, R. M.; Ozkaya, D.; Sheridan, J.; Chater, R. Effects of Water Vapour on Electron and Ion Beam Deposited Platinum. *Microsc. Microanal.* **2004**, *10* (S02), 1122–1123.

(29) Roberts, N. A.; Fowlkes, J. D.; Magel, G. A.; Rack, P. D. Enhanced Material Purity and Resolution via Synchronized Laser Assisted Electron Beam Induced Deposition of Platinum. *Nanoscale* **2013**, *5* (1), 408–415.

(30) Roberts, N. A.; Magel, G. A.; Hartfield, C. D.; Moore, T. M.; Fowlkes, J. D.; Rack, P. D. In Situ Laser Processing in a Scanning Electron Microscope. *J. Vac. Sci. Technol. A Vacuum, Surfaces, Film.* **2012**, *30* (4), No. 041404.

(31) Botman, A.; Mulders, J. J. L.; Weemaes, R.; Mentink, S. Purification of Platinum and Gold Structures after Electron-Beam-Induced Deposition. *Nanotechnology* **2006**, *17* (15), 3779–3785.

(32) Langford, R. M.; Wang, T.-X.; Ozkaya, D. Reducing the Resistivity of Electron and Ion Beam Assisted Deposited Pt. *Microelectron. Eng.* **2007**, *84* (5–8), 784–788.

(33) Frabboni, S.; Gazzadi, G. C.; Felisari, L.; Spessot, A. Fabrication by Electron Beam Induced Deposition and Transmission Electron Microscopic Characterization of Sub-10-Nm Freestanding Pt Nanowires. *Appl. Phys. Lett.* **2006**, *88* (21), 213113–213116.

(34) Plank, H.; Kothleitner, G.; Hofer, F.; Michelitsch, S. G.; Gspan, C.; Hohenau, A.; Krenn, J. Optimization of Postgrowth Electron-Beam Curing for Focused Electron-Beam-Induced Pt Deposits. *J. Vac. Sci. Technol. B* **2011**, *29* (5), 51801–51807.

(35) Mehendale, S.; Mulders, J. J. L.; Trompenaars, P. H. F. A New Sequential EBID Process for the Creation of Pure Pt Structures from MeCpPtMe3. *Nanotechnology* **2013**, *24* (14), No. 145303.

(36) Plank, H.; Noh, J. H. J. H.; Fowlkes, J. D. J. D.; Lester, K.; Lewis, B. B. B.; Rack, P. D. P. D. Electron-Beam-Assisted Oxygen Purification at Low Temperatures for Electron-Beam-Induced Pt Deposits: Towards Pure and High-Fidelity Nanostructures. *ACS Appl. Mater. Interfaces* **2014**, *6* (2), 1018–1024.

(37) Stanford, M. G.; Lewis, B. B.; Noh, J. H.; Fowlkes, J. D.; Roberts, N. A.; Plank, H.; Rack, P. D. Purification of Nanoscale Electron-Beam-Induced Platinum Deposits via a Pulsed Laser-Induced Oxidation Reaction. *ACS Appl. Mater. Interfaces* **2014**, *6* (23), 21256–21263.

(38) Geier, B.; Gspan, C.; Winkler, R.; Schmied, R.; Fowlkes, J. D.; Fitzek, H.; Rauch, S.; Rattenberger, J.; Rack, P. D.; Plank, H. Rapid and Highly Compact Purification for Focused Electron Beam Induced Deposits: A Low Temperature Approach Using Electron Stimulated H2O Reactions. *J. Phys. Chem. C* **2014**, *118* (25), 14009–14016.

(39) Burbridge, D. J.; Gordeev, N. Proximity Effects in Free-Standing EBID Structures. *Nanotechnology* **2009**, *20*, No. 285308.

(40) Plank, H.; Gspan, C.; Dienstleder, M.; Kothleitner, G.; Hofer, F. The Influence of Beam Defocus on Volume Growth Rates for Electron Beam Induced Platinum Deposition. *Nanotechnology* **2008**, *19* (48), 485302–485309.

(41) Fowlkes, J. D.; Randolph, S. J.; Rack, P. D. Growth and Simulation of High-Aspect Ratio Nanopillars by Primary and Secondary Electron-Induced Deposition. *J. Vac. Sci. Technol. B* **2005**, *23*, 2825–2832.

(42) Fowlkes, J. D.; Winkler, R.; Lewis, B. B.; Stanford, M. G.; Plank, H.; Rack, P. D. Simulation-Guided 3D Nanomanufacturing via Focused Electron Beam Induced Deposition. *ACS Nano* **2016**, *10* (6), 6163–6172.

(43) Schmidt, F.-P.; Ditlbacher, H.; Hohenester, U.; Hohenau, A.; Hofer, F.; Krenn, J. R. Dark Plasmonic Breathing Modes in Silver Nanodisks. *Nano Lett.* **2012**, *12* (11), 5780–5783.

(44) Mølhave, K.; Madsen, D. N.; Dohn, S.; Bøggild, P. Constructing, Connecting and Soldering Nanostructures by Environmental Electron Beam Deposition. *Nanotechnology* **2004**, *15* (8), 1047–1053.

(45) Bret, T.; Utke, I.; Hoffmann, P.; Abourida, M.; Doppelt, P. Electron Range Effects in Focused Electron Beam Induced Deposition of 3D Nanostructures. *Microelectron. Eng.* **2006**, *83* (4–9), 1482–1486.

(46) Winkler, R.; Fowlkes, J.; Szkudlarek, A.; Utke, I.; Rack, P. D.; Plank, H. The Nanoscale Implications of a Molecular Gas Beam during Electron Beam Induced Deposition. *ACS Appl. Mater. Interfaces* **2014**, *6* (4), 2987–2995.

(47) Winkler, R.; Szkudlarek, A.; Fowlkes, J. D.; Rack, P. D.; Utke, I.; Plank, H. Toward Ultraflat Surface Morphologies During Focused Electron Beam Induced Nanosynthesis: Disruption Origins and Compensation. *ACS Appl. Mater. Interfaces* **2015**, *7* (5), 3289–3297.

(48) Schmied, R.; Fowlkes, J. D.; Winkler, R.; Rack, P. D.; Plank, H. Fundamental Edge Broadening Effects during Focused Electron Beam Induced Nanosynthesis. *Beilstein J. Nanotechnol.* **2015**, *6* (1), 462–471.

(49) Arnold, G.; Timilsina, R.; Fowlkes, J. D.; Orthacker, A.; Kothleitner, G.; Rack, P. D.; Plank, H. Fundamental Resolution Limits during Electron Induced Direct Write Synthesis. *ACS Appl. Mater. Interfaces* **2014**, *6*, 7380–7387.

(50) Plank, H.; Smith, D. A.; Haber, T.; Rack, P. D.; Hofer, F. Fundamental Proximity Effects in Focused Electron Beam Induced Deposition. *ACS Nano* **2012**, *6* (1), 286–294.

(51) Winkler, R.; Geier, B.; Plank, H. Spatial Chemistry Evolution during Focused Electron Beam-Induced Deposition: Origins and Workarounds. *Appl. Phys. A Mater. Sci. Process.* **2014**, *117* (4), 1675-1688.

(52) Plank, H.; Smith, D. A.; Haber, T.; Rack, P. D.; Hofer, F. Fundamental Proximity Effects in Focused Electron Beam Induced Deposition. *ACS Nano* **2012**, *6* (1), 286–294.

(53) Stockman, M. Nanofocusing of Optical Energy in Tapered Plasmonic Waveguides.

Phys. Rev. Lett. **2004**, *93* (13), No. 137404.

(54) Hohenau, A.; Ditlbacher, H.; Lamprecht, B.; Krenn, J. R.; Leitner, A.; Aussenegg, F. R. Electron Beam Lithography, a Helpful Tool for Nanooptics. *Microelectron. Eng.* **2006**, *83* (4–9), 1464–1467.

(55) Nelayah, J.; Kociak, M.; Stéphan, O.; García de Abajo, F. J.; Tencé, M.; Henrard, L.; Taverna, D.; Pastoriza-Santos, I.; Liz-Marzán, L. M.; Colliex, C. Mapping Surface Plasmons on a Single Metallic Nanoparticle. *Nat. Phys.* **2007**, *3* (5), 348–353.

(56) Schaffer, B.; Hohenester, U.; Trügler, A.; Hofer, F. High-Resolution Surface Plasmon Imaging of Gold Nanoparticles by Energy-Filtered Transmission Electron Microscopy. *Phys. Rev. B* **2009**, *79* (4), No. 41401.

(57) Haberfehlner, G.; Trügler, A.; Schmidt, F. P.; Hörl, A.; Hofer, F.; Hohenester, U.; Kothleitner, G. Correlated 3D Nanoscale Mapping and Simulation of Coupled Plasmonic Nanoparticles. *Nano Lett.* **2015**, *15* (11), 7726–7730.

(58) Jeanguillaume, C.; Colliex, C. Spectrum-Image: The next Step in EELS Digital Acquisition and Processing. *Ultramicroscopy* **1989**, *28* (1–4), 252–257.

(59) Schmidt, F.-P.; Ditlbacher, H.; Hohenester, U.; Hohenau, A.; Hofer, F.; Krenn, J. R. Universal Dispersion of Surface Plasmons in Flat Nanostructures. *Nat. Commun.* **2014**, *5*, No. 3604.

(60) Bosman, M.; Zhang, L.; Duan, H.; Tan, S. F.; Nijhuis, C. A.; Qiu, C.-W.; Yang, J. K. W. Encapsulated Annealing: Enhancing the Plasmon Quality Factor in Lithographically-Defined Nanostructures. *Sci. Rep.* **2014**, *4*, No. 5537.

Figure 1

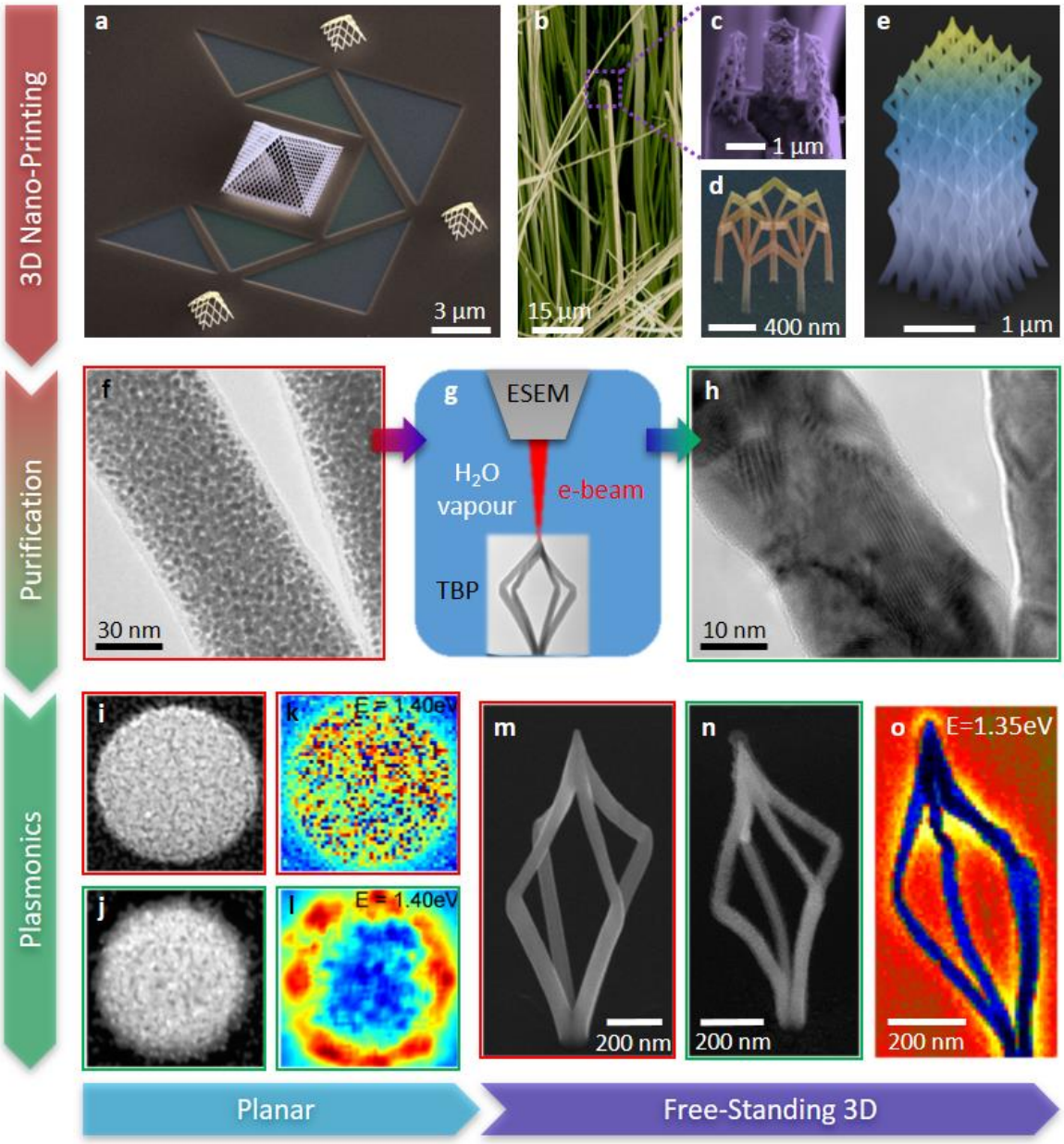

Figure 1: The route towards 3D plasmonic Au structures. (a-e) demonstrates FEBIDs 3D nano-printing capabilities via SEM images: (a) replica of the glass pyramid of the Louvre with nano-branch diameters of ~50 nm; (b-c) demonstrating FEBIDs direct-write capabilities of complex 3D nano-structures on highly exposed, non-flat areas (mineralic nanowires); (d-e) on-demand fabrication of free-standing nano-architectures which are extremely challenging or even impossible with alternative techniques on that scale. (f-h) illustrates the approach towards purely metallic 3D objects imaged via bright-field TEM: while as-deposited FEBID materials reveal the typical nano-granular composition of metal grains (dark spots) embedded in a carbon matrix (f), the latter is entirely removed by e-beam exposure in water vapour environments (g) leading to highly compact, crystalline gold structures (h). This paves the way towards planar plasmonics in a first step, illustrated in (i-l): the application of the purification process (g) transforms as-deposited Au-C disks (i, HAADF image of a 400

nm wide disk) into pure Au materials (j) switching from no plasmonic response (k, STEM EEL map at 1.4 eV taken from i) to a strong plasmonics activity (l). After confirming the plasmonic suitability of FEBID based materials in principle, the process is transferred to free-standing 3D tetragonal-bipyramids (TBP, see also inset in g): after intial 3D nano-printing of TBP's (m, tilted SEM image), the structures are purified with the same approach (g) leading to compact 3D Au structures (n, tilted SEM image), further investigated via STEM EELS measurements which reveal strong plasmonic activity for FEBID based true 3D nano-architectures (o, STEM EEL map at 1.35 eV). Note the surface contamination after purification (n) is a SEM-only feature and absent if directly using TEM.

Figure 2

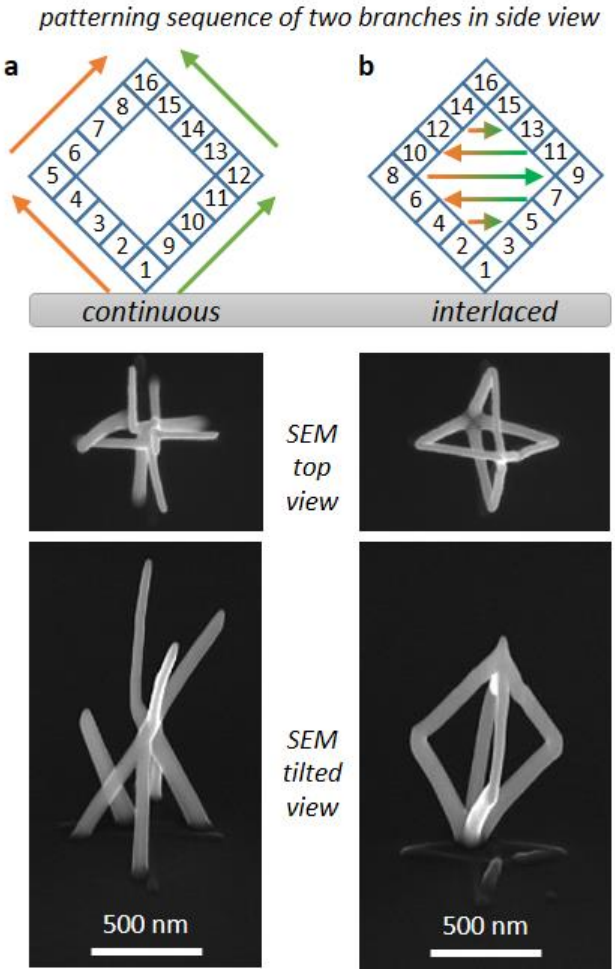

Figure 2: Application of advanced patterning strategies to achieve predictable and reproducible 3D nano-architectures. (a) in a continuous growth strategy, each single branch is grown individually as outlined in the top scheme (see numbers and arrows). The result are entirely collapsed structures as evident by top- and side view SEM images.To get stable 3D growth as shown in the SEM images in (b), an interlaced patterning sequence is introduced which grows all four branches almost simultaneously by systematic patterning jumps, as indicated on top of (b) for a two branch structure in a side view (see also arrows). Note, both structures used same number of patterning points, DTs, PoPs and total fabrication times as only the patterning sequence has been changed which demonstrates the high importance for the fabrication of more complex structures as shown in Figure 1a-e.

Figure 3

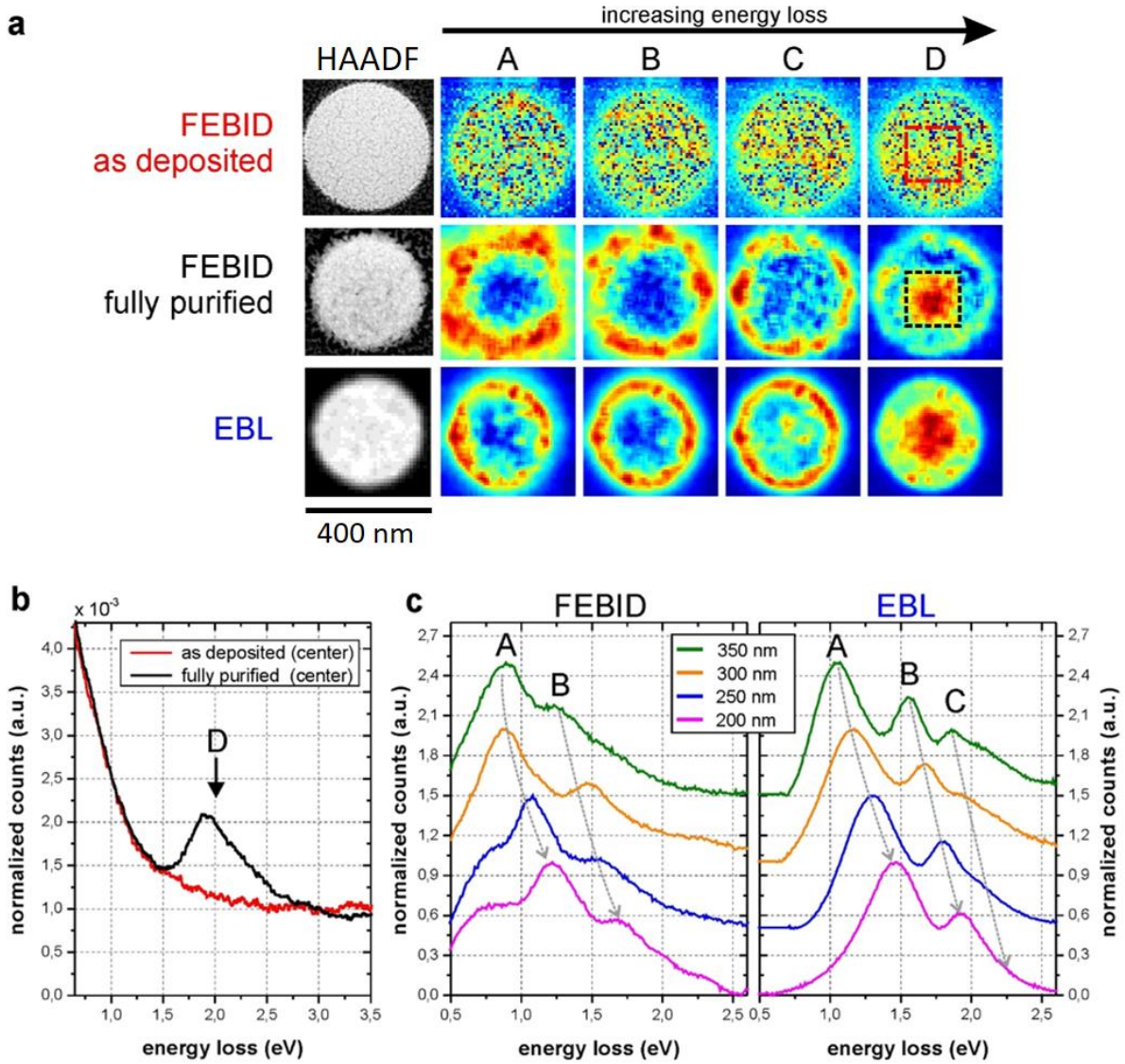

Figure 3: EEL maps and spectra of FEBID and EBL disks. (a) HAADF survey images (left column) together with corresponding EEL maps at increasing electron loss energies (column A – D) for as-deposited gold disk (thickness 60 nm, diameter 400 nm, top row), fully purified disk (height / diameter decrease to 30 nm / 350 nm, central row) and EBL gold disks (same dimensions as for purified disk, bottom row). (b), direct comparison of EEL spectra acquired at the centre of as-deposited and fully purified FEBID disks (see (a), column D). (c), EEL spectra acquired along the disk circumference of fully purified FEBID and EBL disks for different disk diameters.

Figure 4

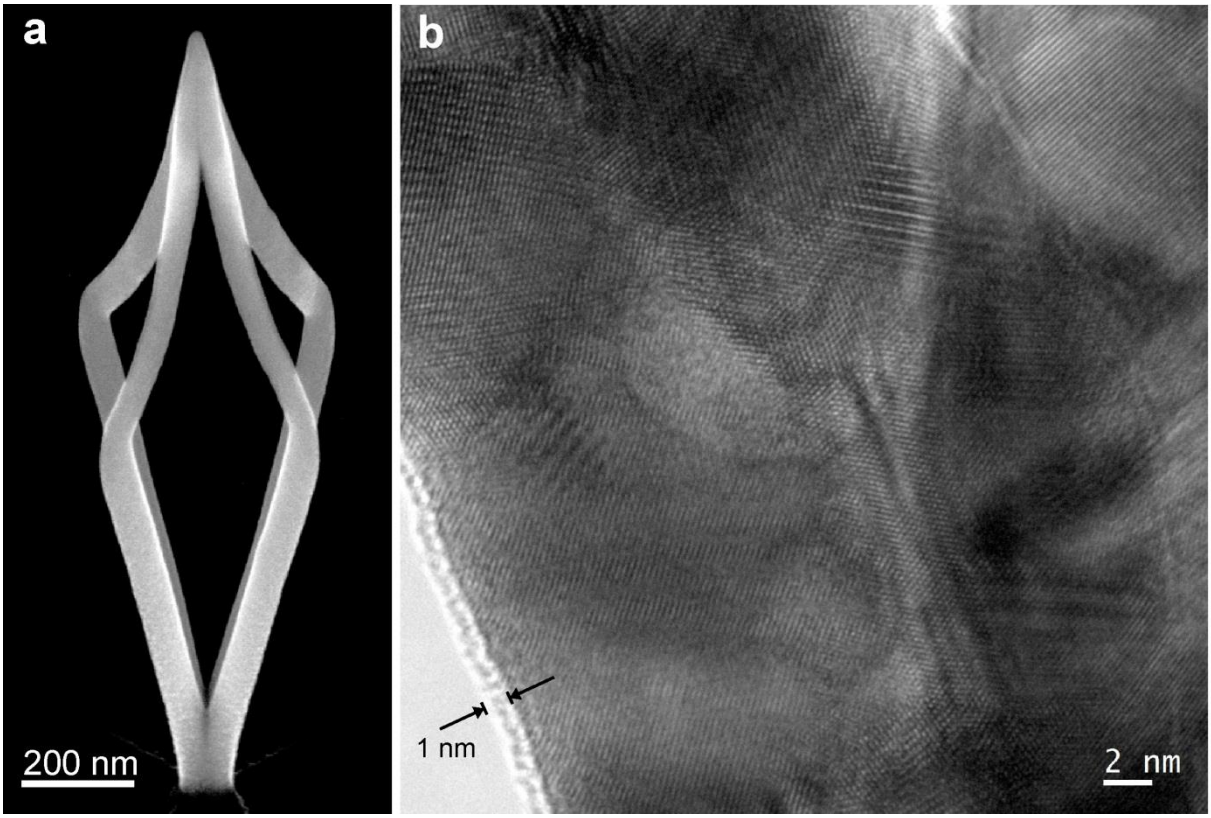

Figure 4: Purification of free-standing gold-nanostructures. (a) purified tetragonal bipyramid geometry. (b) High-resolution TEM image of a fully purified 3D-FEBID structure exposing highly compact and crystalline gold branches with diameters below 25 nm and surface contamination layers of less than 1 nm.

Figure 5

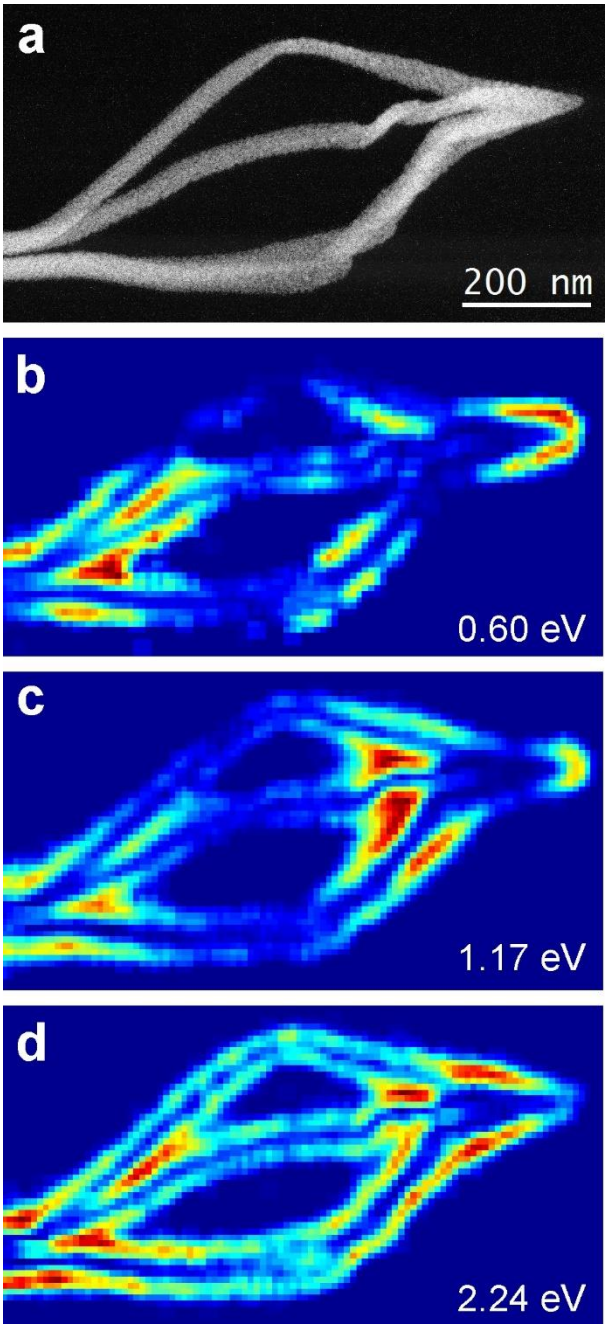

Figure 5: Plasmonic response of FEBID based 3D Au nanostructures. HAADF survey image (a) together with EEL maps revealing the plasmonic activities at different electron loss energies (see indications in b-d and also see Supporting Video). Noteworthy are the widely symmetric appearances which reveal the high precision after initial fabrication and also the minimally invasive character of the material purification.

Figure 6

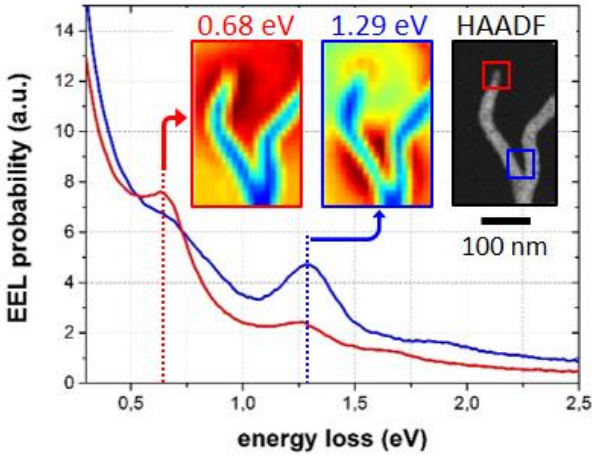

Figure 6: unprocessed EEL spectra on a fully purified 3D Au structure taken from the tip region (red) and the branched area (blue) as indicated in the HAADF survey image top right. While the clear appreance of plasmon peaks in uncorrected spectra indicate the high material quality, the EEL maps insets give laterally resolved information at energy losses of 0.68 eV and 1.29 eV confirming the highly localized plasmonic acitivites.